Meta-modeling of high-fidelity FEA simulation for efficient product and process design in additive manufacturing

Lening Wang[a], Xiaoyu Chen[a], Sungku Kang[a], Xinwei Deng[b], Ran Jin[a,*]

[a] *Grado Department of Industrial and Systems Engineering, Virginia Tech, United States*
[b] *Department of Statistics, Virginia Tech, United States*

ARTICLE INFO

ABSTRACT

Finite element analysis (FEA) has been widely adopted to identify potential defects in additive manufacturing (AM) processes. For personalized product realization, it is necessary to validate a number of heterogeneous product and process designs before or during manufacturing by using FEA. Multi-fidelity FEA simulations can be readily implemented with different capabilities in terms of simulation accuracy. However, due to its complexity, high-fidelity FEA simulation is time-consuming and decreases the efficiency of product realization in AM, while low-fidelity FEA simulation has fast computation speed yet limited capability. Hence, our objective is to improve the capability of FEA by providing an efficient data-driven model. In this research, a Gaussian process-constrained general path model is proposed to approximate the high-fidelity FEA simulation results based on low-fidelity results voxel-by-voxel. The proposed model quantifies the heterogeneous discrepancies between low- and high-fidelity FEA simulation results by incorporating the product design information (e.g., Cartesian coordinates of deposition sequence) and process design information from inputs of FEA simulation (e.g., input heat). Therefore, it enables the validation of new product and process designs based on the simulation results with the desired capability in a timely manner. The advantages of the proposed method are illustrated by FEA simulations of the fused deposition modeling (FDM) process with two levels of fidelity (i.e., low- and high-fidelity).

1. Introduction

In recent years, additive manufacturing (AM) becomes a driving force for personalized product realization [1], such as customized brackets in aircraft and automotive manufacturing [2], and biomedical devices conforming to patient anatomy [3]. Despite advancements in AM for facilitating personalized manufacturing, it is important to validate a number of heterogeneous products and process designs *in a timely manner*. In the literature, there are usually two ways to validate AM designs: i) traditional run-to-run studies to physically quantify the quality/functional performance of the product and process designs through the design of experiments (DOE) [4–6]; and ii) high-fidelity simulations to predict the corresponding quality/functional performance of designs [7–9]. The DOE approach can be inefficient and expensive as different customized AM designs have different underlying mechanisms [10]. For each individual design, one needs to physically conduct DOE to collect sufficient samples to estimate the model. Alternatively, simulations have been widely adopted to identify potential defects in AM processes by simulating the physical mechanisms of the manufacturing processes [7–9]. However, a high-fidelity FEA

simulation can be computationally expensive and thus cannot be easily used to validate AM designs in a timely manner. On the other hand, a low-fidelity simulation provides affordable computation time. The accuracy of low-fidelity simulations might not be satisfactory due to their low meshing resolutions.

In this work, the objective is to improve the accuracy of the low-fidelity FEA simulation results by predicting high-fidelity simulation results to facilitate and accelerate the AM design validation with heterogeneous product and process features (e.g., different geometries or process settings). Let us take the example of the thermal distribution analysis of the fused deposition modeling (FDM), which is a material extrusion AM process. An infrared camera cannot capture the external spatial-temporal thermal distribution of the product since the extruder will block the vision of infrared camera during the process. In addition, the internal thermal distribution is not measurable. However, the thermal distribution is very important in the FDM process as it is closely related to the quality/defect of AM products, such as residual stress [11] and geometric deviation [12]. In such a case where sensing capability is limited, FEA simulation can help the validation of product and process designs as well as understanding the process-quality

---

Table 1
Examples of low- and high-fidelity FEA simulation based on a National Institute of Standards and Technology (NIST) standard design [13].

Variable name	Low-fidelity	High-fidelity
Meshing size (maximum)	1 mm	0.3 mm
No. of elements	16743	424743
Computation time	30 min	21 h

relationship in AM processes [13]. There are different levels of fidelity for FEA simulations, as compared briefly in Table 1 for a 3D transient thermal field evolution FEA simulation in FDM with the same design.

A high-fidelity FEA simulation can be computationally intensive (more than 20 hours for a single product with one specific process design), which cannot be affordable to validate a large number of personalized AM designs with heterogeneous geometries and process settings. Thus it is useful to develop a model that can approximate the high-fidelity FEA simulation results based on the low-fidelity FEA results. Such a model can boost the capability of low-fidelity FEA simulation and efficiently facilitate the personalized product and process design validation (i.e., identifications of manufacturability or functionality for varied geometries under different process setting combinations) in AM.

There are a few challenges in modeling the relationship between low- and high-fidelity FEA simulation results. First, along the deposition sequence, the length of thermal history for each location varies in an AM process. For example, Fig. 1 demonstrates a 3D transient FEA for the thermal field evolution results of three locations (i.e., A, B and C) on

a square product which is modified based on the NIST standard part [14] and built by PLA in a FDM process [13]. Arrows represent the deposition sequence of the FDM process. In Fig. 1, it can be observed that each location has a different length of thermal history. This is because that each location on the product is deposited at a different time point following the pre-defined deposition sequence. According to the sequence shown in Fig. 1(a), when location A has been deposited on the platform, B and C have not been deposited yet. This inconsistency of thermal history sequences length among different locations restricts many existing data-driven methods [15,16] with the assumption of the same sequence length. Second, the discrepancies between low- and high-fidelity FEA simulation results are heterogeneous among different locations over time. As shown in Fig. 1(a), in terms of geometries in one layer, the Euclidean distance between point A and point B is the same as that between point A and point C. However, it can be found that the discrepancy patterns between low- and high-fidelity FEA simulation results vary along the deposition sequence. For example, the predicted thermal evolution histories from low-fidelity FEA simulation results in Fig. 1(b) and (c) have relatively low errors by comparing with high-fidelity results. But for Fig. 1(d), it can be observed at the beginning of the predicted thermal evolution history, the accuracy of the low-fidelity simulation is very inaccurate. Moreover, in the middle of these three predicted thermal histories, it can be seen that for Fig. 1(b) and (c), the prediction results from the high-fidelity simulation are larger than the low-fidelity simulation, while for Fig. 1(d), it is opposite. These heterogeneous discrepancies are significant since the numerical value of the difference between low- and high-fidelity simulation is larger than the simulation accuracy (i.e., 5 Kelvin (K) in terms of root-mean-
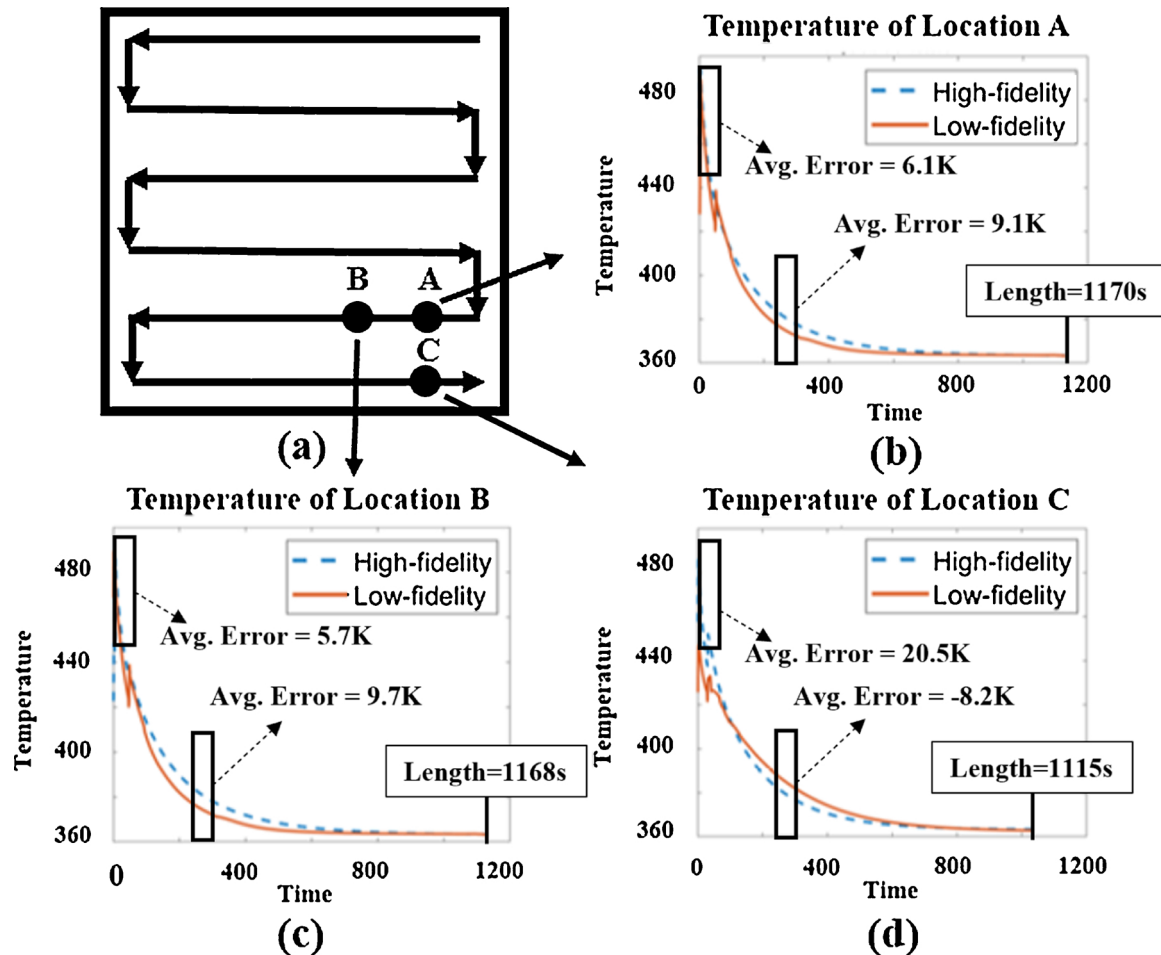

Fig. 1. Temperatures from different locations in a FDM process for high- and low-fidelity simulation.((a) Deposition sequence; (b) Simulation results for location A; (c) Simulation results for location B; (d) Simulation results for location C).

squared-error) [17]. Therefore, even if two locations have the same Euclidean distance with the same reference point, the discrepancies are heterogeneous and cannot be modeled by a stationary process. This heterogeneity is difficult to be quantified by functional data analysis methods with the assumption of thermal history sequences having similar patterns in temporal correlation [18]. Third, one-of-a-kind products in highly personalized manufacturing provide limited historical data to effectively support the model estimation by using most of the existing data-driven models.

Therefore, the authors propose a Gaussian process-constrained general path (GPGP) model to improve the capability of low-fidelity FEA simulation in terms of simulation accuracy and computational efficiency. The GPGP model can effectively predict the high-fidelity FEA simulation results based on the low-fidelity simulation by modeling the heterogeneous discrepancies between low- and high-fidelity results via general path models. As shown in Fig. 1, the AM product can be decomposed into individual locations, and data at each location are treated as one sample in this study. For different locations, general path models are estimated with Gaussian process model-based constraints to quantify correlation among locations. When two paths have similar covariates, they tend to have similar discrepancy patterns, which lead to highly correlated model coefficients (see Section 4 for validation). In this manner, the estimated GPGP model (trained from the historical data in other designs) can make a prediction on the high-fidelity FEA simulation results for a new design based on low-fidelity simulation with the use of the product design and process design features.

There are several advantages of the proposed method. First, the proposed method is to model discrepancies between low- and high-fidelity FEA simulation results at each individual location regardless of lengths. It can mitigate the dependency on geometric characteristics of products to improve the generality of the model. Second, we use the general path model to parameterize discrepancies between low- and high-fidelity FEA simulation results at each location through one or several paths. The general path model considers a general function form (e.g., polynomial function) with few coefficients to approximate a sequence [19]. Note that the discrepancy between low- and high-fidelity simulation within each path can be roughly approximated by a general function form (e.g., a polynomial function). Therefore, the heterogeneity of discrepancies among locations is decomposed into individual discrepancies within each path and further modeled by a parametric model. Third, recall that the simulation results shown in Fig. 1(b) and (c), and define the low- and high-fidelity simulation results from two locations as two paths. Since the discrepancies between the two paths are similar, it also leads to similar model coefficients of the general path models. This similarity can be represented by product design information (e.g., Cartesian coordinates of deposition sequence) and process design information from inputs of low-fidelity FEA simulation (e.g., input heat). To enforce similar correlation structures among general path models and correlation structure among covariates in different paths, Gaussian process models are adopted as constraints in the estimation of coefficients for individual general path models. In a short summary, the proposed GPGP model can facilitate the validation for heterogeneous AM designs by efficiently reducing the computational cost of FEA simulation with reasonable accuracy based on the historical simulation results. Benefit from the flexibility of FEA simulation, the proposed model can be potentially extended to other AM processes which have a similar mechanism (i.e., layer-wise deposition of material) such as selective laser melting (SLM).

The rest of the article is organized as follows. Section 2 demonstrates the state-of-the-art of FEA simulations in AM processes and statistical methods to improve the FEA simulation accuracy. Section 3 introduces the proposed GPGP model in detail. Section 4 demonstrates the proposed method via the case study of thermal field simulation in the FDM process. Lastly, Section 5 summarizes the contributions of this work and discuss future work.

2. Literature review

In the literature, the FEA simulation for AM processes has been intensively studied. For example, Heigel et al. introduced a thermo-mechanical FEA simulation model to predict the thermal gradient of the product in AM processes [20]. Chen et al. proposed a multiscale process FEA simulation framework to efficiently and accurately estimate the residual distortion and stress of AM products based on the modified inherent strain model [21]. Bhandari and Lopez-Anido introduced a space frame lattice and shell FEA simulation model to estimate the linearly elastic responses (i.e., elastic modulus, shear modulus, and Poisson's ratio) and further support the design and optimize of AM products [22]. Kao et al. presented a study to investigate the bending behaviors of a bi-material structure (BMS) built by the AM process via finite element analysis, which can help to validate the overall mechanical properties of the composite [23]. In summary, there are many effective FEA methods to accurately predict the product quality of AM product and further validate the design in different aspects (e.g., thermal distribution, mechanical properties, functionalities, and etc.). However, the computational intensity of these methods is significantly high as shown in Table 1. Even though there are some studies to improve the computation efficiency of FEA methods for AM processes such as utilizing the Graphical Processing Units (GPU) to accelerate the simulation [24], it still needs to re-compile the existing methods and also time-consuming and complicated. Therefore, how to improve the efficiency of the FEA simulation for AM processes without sacrificing the accuracy and abandoning the existing simulation framework is important to better support product and process design validation in AM.

On the other hand, various statistical methods have been proposed to improve the FEA simulation accuracy. One type of methods is computer model calibration [25–27], which can statistically model the variability of computer experiments, calibrate simulation parameters, and compensate inadequate physics in a simulator [27,28]. These methods have been widely used to reduce the uncertainty in the computer model by optimizing calibration parameters, such as the uncertainty introduced from the initial conditions and the important physical parameters [28]. However, no calibration parameter can be defined to quantify the heterogeneous discrepancy between low- and high-fidelity FEA simulation results. Besides, data-driven models have been proposed to enhance the accuracy of low-fidelity experimental or simulation results based on non-parametric model frameworks, such as hierarchical Gaussian process model [29–33]. However, these methods concentrate on limited existing types of product and process designs. Therefore, it is unclear how to model product and process designs of free-form. On the other hand, transfer learning models can help to transfer the knowledge from one domain to another domain, where domains may share similar-but-non-identical distributions [34–36]. However, large sample sizes from the source and target domain are required to train an accurate model for the target domain. In AM, where the products are typically one-of-a-kind, the requirement of adequate samples may not be affordable. With a limited sample size, it might not be efficient to identify the amount of information or what the common features can be transferred from one product to another product.

3. Methodology

In this section, the proposed GPGP model is introduced. In order to clarify the scope of this study, three assumptions are made: 1) the low- and high-fidelity FEA simulation results are collected from the FEA simulations of same manufacturing process. The high-fidelity results are collected from the FEA simulation with relatively high meshing resolutions after the calibration [25]. The low-fidelity results are collected from the FEA simulation with lower meshing resolutions after the calibration [25]; 2) for each path defined by a group of data from low- and high-fidelity FEA simulation results, the relationship between low- and high-fidelity results can be quantified as a general path model with

a first-order polynomial form; and 3) model coefficients of general path models share a similarity structure that can be quantified by product design information and process design information among different paths. These assumptions will be validated in Section 4.

In order to reduce the possible numerical errors from FEA simulation for each location, the weighted average of simulation results among spatially adjacent locations is employed to interpolate the FEA simulation results for each location along the deposition sequence [37,38]. This interpolation procedure aims at registering the low- and high-fidelity FEA simulation results together in the same set of locations since their meshing resolutions are different.

3.1. Gaussian process-constrained general path model

Denote a group of high-fidelity FEA simulation results (i.e., temperatures) and corresponding low-fidelity results (i.e., temperatures) for the ith path as $(\boldsymbol{y}_i, \boldsymbol{x}_i)$, where $i = 1, ..., m$; m is the total number of paths; $\boldsymbol{y}_i = [y_{i1}, ..., y_{ij}, ..., y_{it_i}]^\top$; $\boldsymbol{x}_i = [x_{i1}, ..., x_{ij}, ..., x_{it_i}]^\top$; $j = 1, ..., t_i$; t_i is the total time-stamps for path i. Note that there can be multiple paths in one location, as illustrated in Section 4.2. To model the relationship between low- and high-fidelity FEA simulation results for path i at time-stamp j, a first-order polynomial form of general path model is employed based on the assumption. Other terms can be easily adopted in this model framework, such as lags or differentiation information of data [39]. Specifically, the relationship between low- and high-fidelity FEA simulation results for path i at time-stamp j can be modeled as follows:

$$y_{ij} = \beta_{i0} + \beta_{i1}x_{ij} + \varepsilon_{ij}, \ \varepsilon_{ij} \sim t_\nu(0, \sigma^2), \tag{1}$$

where $\boldsymbol{\beta}_0 = [\beta_{10}, ..., \beta_{i0}, ..., \beta_{m0}]^\top$ and $\boldsymbol{\beta}_1 = [\beta_{11}, ..., \beta_{i1}, ..., \beta_{m1}]^\top$ are the corresponding vectors of model coefficients; For the error term ε_{ij}, we employ the Student-t distribution which has a fatter tail to improve the robustness of the general path model among different paths, in contrast with using the normal distribution [40]. Note that the outliers may be caused by irregular element shapes or numerical errors from the low-fidelity FEA simulation results. σ^2 is the variance of the error term.

Recall the assumption for model coefficients, we enforce the similarity structure among model coefficients by adopting Gaussian process models as constraints in the estimation of general path models as follows:

$$\boldsymbol{\beta}_0(Z)|\tau_0, \boldsymbol{l}_0 \sim \text{GP}(\mu_0 \boldsymbol{1}_m, K_0),$$
$$\boldsymbol{\beta}_1(Z)|\tau_1, \boldsymbol{l}_1 \sim \text{GP}(\mu_1 \boldsymbol{1}_m, K_1), \tag{2}$$

where Z are the covariates, including summary statistics of product design information (e.g., Cartesian coordinates of deposition sequence) and process design information from the inputs of low-fidelity FEA simulation (e.g., input heat); The summary statistics include path length, standard deviation, skewness, kurtosis, mean value, the average of magnitude, entropy, max and min value, max value for 2nd differential of path, max value for 3rd differential of path, and variance for 2nd differential of path; τ_0 and τ_1 are amplitude factors of kernel functions; w is the total number of covariates; $\boldsymbol{l}_0 = [l_{01}, ..., l_{0w}]^\top$ and $\boldsymbol{l}_1 = [l_{11}, ..., l_{1w}]^\top$ are lengthscale factors of kernel functions; μ_0 and μ_1 are the mean value for the model coefficients. $\boldsymbol{1}_m$ is an m-dimensional column vector of 1s. In this study, the exponential kernel function [41] is selected. It is an universal kernel that can be integrated efficiently with only two hyperparameters [42]. Other kernel functions such as Matérn kernel, rational quadratic kernel, and non-stationary kernels such as dot-product kernel can also be easily employed in this framework [43]. K_0 and K_1 are the covariance matrices, where $K_0(Z, Z) = (k_0(\boldsymbol{z}_i, \boldsymbol{z}_{i'}))_{m \times m}$, $K_1(Z, Z) = (k_1(\boldsymbol{z}_i, \boldsymbol{z}_{i'}))_{m \times m}$. To calculate the covariance matrix, specifically, the kernel functions k_0 and k_1 can be written as follows:

$$k_0(\boldsymbol{z}_i, \boldsymbol{z}_{i'}) = \tau_0^2 \exp\left(-\sum_{s=1}^{w} \frac{(z_{is} - z_{i's})^2}{2l_{0s}^2}\right),$$

$$k_1(\boldsymbol{z}_i, \boldsymbol{z}_{i'}) = \tau_1^2 \exp\left(-\sum_{s=1}^{w} \frac{(z_{is} - z_{i's})^2}{2l_{1s}^2}\right), \tag{3}$$

where $\boldsymbol{z}_i = [z_{i1}, ..., z_{iw}]^\top$ and $\boldsymbol{z}_{i'} = [z_{i'1}, ..., z_{i'w}]^\top$ are vectors of covariates for path i and i', respectively; $Z = [\boldsymbol{z}_1, \boldsymbol{z}_2, ..., \boldsymbol{z}_m]^\top$. The proper posteriors rely on proper prior of hyperparameters [41]. Therefore, the following priors are chosen [29]:

$$p(\tau_0) \sim \text{IG}(\alpha_0, \gamma_0), \ p(\tau_1) \sim \text{IG}(\alpha_1, \gamma_1),$$
$$p(l_{0s}) \sim \text{IG}(\alpha_{0s}, \gamma_{0s}), \ p(l_{1s}) \sim \text{IG}(\alpha_{1s}, \gamma_{1s}),$$
$$p(\mu_0) \sim \mathcal{N}(a_0, b_0^2), \ p(\mu_1) \sim \mathcal{N}(a_1, b_1^2), \ p(\sigma^2) \sim \text{IG}(\alpha_2, \gamma_2), \tag{4}$$

where $s = 1, ..., w$; $\text{IG}(\alpha, \gamma)$ is the inverse gamma distribution [44] parameterized by shape α and scale γ to serve as an non-informative prior with finite support to constrain the model coefficients within a certain region; $\mathcal{N}(a, b^2)$ is the normal distribution parameterized by mean a and variance b^2.

3.2. Model estimation and inference

The traditional Markov chain Monte Carlo (MCMC) samplers, such as Gibbs [44], usually lead to a large fraction of rejected samples. Therefore, in this study, the Hamiltonian Monte Carlo based No-U-Turn Sampler (NUTS) [45] is employed for model estimation. Specifically, the probability density function of Eq. (1) can be shown as follows:

$$p(y_{ij}|x_{ij}, \beta_{i0}, \beta_{i1}, \nu, \sigma^2)$$
$$= \frac{\Gamma\left(\frac{\nu+1}{2}\right)}{\Gamma\left(\frac{\nu}{2}\right)\sqrt{\nu\pi\sigma^2}}\left(1 + \frac{(y_{ij} - \beta_{i0} - \beta_{i1}x_{ij})^2}{\nu\sigma^2}\right)^{-(\nu+1)/2}, \tag{5}$$

where ν is the degrees of freedom with a prior information: $\frac{1}{\nu} \sim \mathcal{U}(0, 0.5)$ [40], $\mathcal{U}(\cdot, \cdot)$ is a uniform distribution. Moreover, the probability density functions of Eq. (2) can be shown as follows:

$$p(\boldsymbol{\beta}_0|\mu_0 \boldsymbol{1}_m, K_0) =$$
$$(2\pi)^{-m/2}|K_0|^{-1/2}\exp\left(-\frac{1}{2}(\boldsymbol{\beta}_0 - \mu_0 \boldsymbol{1}_m)^\top K_0^{-1}(\boldsymbol{\beta}_0 - \mu_0 \boldsymbol{1}_m)\right),$$
$$p(\boldsymbol{\beta}_1|\mu_1 \boldsymbol{1}_m, K_1) =$$
$$(2\pi)^{-m/2}|K_1|^{-1/2}\exp\left(-\frac{1}{2}(\boldsymbol{\beta}_1 - \mu_1 \boldsymbol{1}_m)^\top K_1^{-1}(\boldsymbol{\beta}_1 - \mu_1 \boldsymbol{1}_m)\right). \tag{6}$$

By collecting all the hyperparameters into $\theta = [\tau_0, \boldsymbol{l}_0, \mu_0, \tau_1, \boldsymbol{l}_1, \mu_1, \sigma^2, \nu]$, the predictive density function can be formulated as follows:

$$p(\boldsymbol{y}_1, ..., \boldsymbol{y}_m|\boldsymbol{x}_1, ..., \boldsymbol{x}_m, \theta)$$
$$= \int_{\boldsymbol{\beta}_0, \boldsymbol{\beta}_1} p(\boldsymbol{y}_1, ..., \boldsymbol{y}_m|\boldsymbol{x}_1, ..., \boldsymbol{x}_m, \boldsymbol{\beta}_0, \boldsymbol{\beta}_1, \theta)p(\boldsymbol{\beta}_0, \boldsymbol{\beta}_1|\theta)d\boldsymbol{\beta}_0 d\boldsymbol{\beta}_1. \tag{7}$$

For prediction perspective, the model coefficients $\boldsymbol{\beta}^* = [\beta_0^*, \beta_1^*]$ for a testing sample with covariates $\boldsymbol{z}^*$ can be estimated as follows [43]:

$$p(\beta_0^*|Z, \boldsymbol{z}^*, \tau_0, \boldsymbol{l}_0)$$
$$\sim \mathcal{N}(K_0^*(K_0 + \sigma^2 I_m)^{-1}(\boldsymbol{\beta}_0 - \mu_0 \boldsymbol{1}_m), K_0^{**} - K_0^*(K_0 + \sigma^2 I_m)^{-1}K_0^{*\top}),$$
$$p(\beta_1^*|Z, \boldsymbol{z}^*, \tau_1, \boldsymbol{l}_1)$$
$$\sim \mathcal{N}(K_1^*(K_1 + \sigma^2 I_m)^{-1}(\boldsymbol{\beta}_1 - \mu_1 \boldsymbol{1}_m), K_1^{**} - K_1^*(K_1 + \sigma^2 I_m)^{-1}K_1^{*\top}), \tag{8}$$

where $K_0^* = [k_0(\boldsymbol{z}_1, \boldsymbol{z}^*), ..., k_0(\boldsymbol{z}_m, \boldsymbol{z}^*)]$, $K_1^* = [k_1(\boldsymbol{z}_1, \boldsymbol{z}^*), ..., k_1(\boldsymbol{z}_m, \boldsymbol{z}^*)]$; I_m is the $m \times m$ identity matrix; $K_0^{**} = k_0(\boldsymbol{z}^*, \boldsymbol{z}^*)$, $K_1^{**} = k_1(\boldsymbol{z}^*, \boldsymbol{z}^*)$. Finally, based on the predicted model coefficients of general path model, we can directly feed the low-fidelity FEA simulation results into the equation to predict the high-fidelity FEA simulation results as:

$$\hat{y}_{ij}^* = \beta_{i0}^* + \beta_{i1}^*x_{ij}^*. \tag{9}$$

The procedures of training and testing for the proposed GPGP model
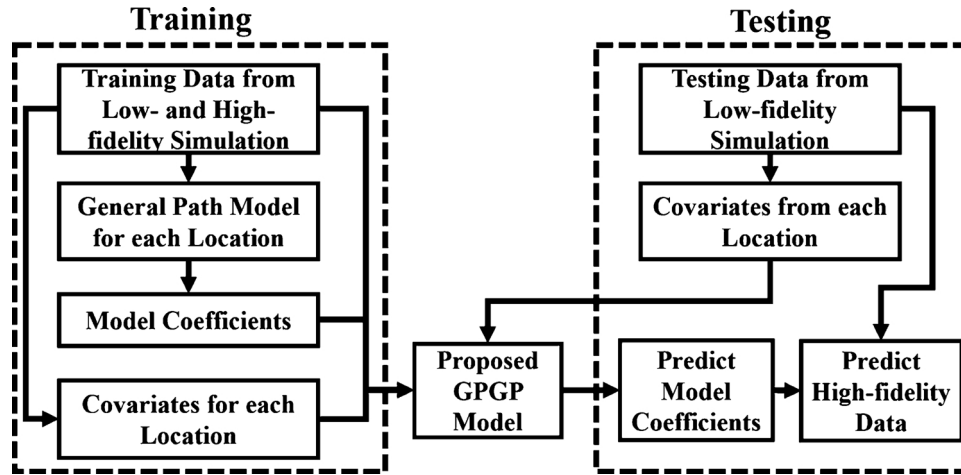
Training

Testing

Fig. 2. A training and testing flowchart for the proposed method.

is shown in Fig. 2. In the training stage, after the spatial-temporal registration for both low- and high-fidelity simulation results, we feed the simulation results and corresponding covariates among different paths into the GPGP model estimator to train the model. On the other hand, in the testing stage, only the results from the low-fidelity FEA simulation and the corresponding covariates are required. Based on the GPGP model, the coefficients of general path model can be predicted, which further predicts the high-fidelity FEA simulation results based on the low-fidelity results.

4. Case study

The objective of this section is to evaluate the prediction performance of the proposed model in comparison with other benchmark methods. The four benchmark methods are Lasso regression [46], tensor regression [47], functional linear regression [18] and variational autoencoder [48]. Furthermore, to validate whether the proposed model can accurately predict the high-fidelity simulation results for a new design based on the historical data, two testing scenarios are employed (i.e., "cross-layers" and "cross-designs"). In addition, the assumptions of the proposed model demonstrated in Section 3 are examined via this case study.

4.1. Experiments setup

In order to evaluate the performance of the proposed GPGP model, we apply the proposed model to a FDM process and conduct the FEA simulation for corresponding manufacturing process under both low- and high-fidelity conditions. Specifically, the FEA simulation is a 3D transient coupled thermo-mechanical FEA model for the thermal field evolution of FDM processes following the simulation procedures by [13]. As shown in Fig. 3, three different product designs are investigated in the case study: standard (d_1), peanut (d_2), and gear (d_3). The size of (d_1) is $44.45 \times 44.45 \times 2.5$ mm^3, which is modified based on the NIST standard part [14]; for (d_2), the contour of peanut is generated according to the Polar coordinate function: $r(\phi) = r_0(1 - \sin\phi\cos\phi)$,
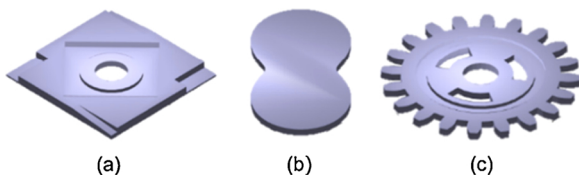
where ϕ is the polar angle $\phi \in [0°, 360°]$; polar radius $r_\phi = 20$ mm. The height of (d_2) is 2 mm; for (d_3), the outer diameter of gear is 55 mm, and the height is 2 mm. The deposition sequences of these three designs contain representative deposition patterns, such as straight lines, circles, sharp corners, concave curves, etc. Note that more complex geometries, such as lattice structure, can be built upon the 2D slices which consist of the aforementioned representative deposition patterns. These designs are thus chosen to validate the potential of the proposed method for extending to more complex geometries in AM. The filament material is semi-crystalline poly-lactic acid (PLA). The simulation and fabrication time for these parts are shown in Table 2. In this 3D transient coupled thermo-mechanical FEA model for the thermal field evolution of the FDM process, the boundary condition for the bottom surface is maintained at the same with the FDM platform denoted as T_{bed}. The convective heat flux for all the other surfaces for transfer heat is q_A, where $q_A = h(T_{bed} - T_{env})$; h is the convective heat transfer coefficient; T_{env} is the environment temperature (i.e., 298.15K). The maximum element size for all three designs are fixed in the same fidelity simulation model (i.e., 1mm for low-fidelity and 0.3mm for high-fidelity as shown in Table 1). Moreover, to better demonstrate the thermal mechanism and characteristic of the deposition region, the meshing size of elements should be fine enough. Such a high density of elements is not required for the regions that far from the deposition region. Therefore, an adaptive meshing method is implemented to adjust the elements' size adaptive to the local temperature gradients during the deposition process [49,50]. An example of adaptive meshing in this case study is shown in Fig. 4. Finally, a Bayesian calibration method [25] is conducted based on actual experimental observations.

4.2. Data pre-processing

In order to better understand the spatial-temporal correlation of simulation results among different locations, as shown in Fig. 5, the simulation results for the standard part (d_1) are organized into a lower triangular matrix. In the lower triangular matrix, each column represents a full thermal history for a specific location (e.g., location n as shown in Fig. 5(a)) during the manufacturing process, and each row

Fig. 3. Three product designs: (a) d_1: standard; (b) d_2: peanut; (c) d_3: gear. (Redrawn from [13] with authors' permission).

Table 2
Simulation time and fabrication time for different designs.

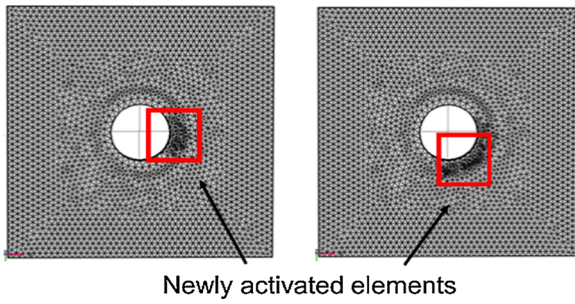|	Standard ($d1$)	Peanut ($d2$)	Gear ($d3$)
Total layer number	10	8	8
Fabrication time	5 min	6 min	5 min
Simulation time (high-fidelity)	22 h	21 h	23 h
Simulation time (low-fidelity)	31 min	33 min	38 min

Newly activated elements

Fig. 4. An Example of the Adaptive Meshing in FEA simulation. (Re-drawn from [13] with authors' permission).

represents a specific time-stamp. For example, as shown in Fig. 5(b), two axes represent the row and the column in the lower triangular matrix, A, B, C, D are four elements in the matrix. Moreover, points $A(j', n)$ and $D(j, n)$ are both temperatures for location n, but at time j' and j respectively. Similarly, point $B(j', n')$ and $C(j, n')$ are temperatures for location n' at different time-stamps j' and j.

From Fig. 5(c), this lower triangular matrix gives a better interpretation of the simulation results since it shows that the adjacent columns tend to have a similar trend of thermal histories after registration according to the deposition sequence. It also can be found that the overall trends of temperatures variation are similar between low- and high-fidelity FEA simulation results. Such a spatial-temporal registration of data preserves the correlation of data over the deposition sequence, which contains all the information from a specific product and process design to better visualize and analyze the low- and high-fidelity FEA simulation results.

For a specific column of the lower triangular matrix from Fig. 5(c), the simulation results are shown on the left of Fig. 6. It can be found that re-heating happened on both low- and high-fidelity FEA simulation results. According to the engineering domain knowledge, the re-heating occurs when the extruder moves back to the neighbor of extruded locations [51]. The thermal energy on the extruder can re-heat its surrounding area rapidly. On the other hand, without re-heating, the temperature of extruded locations should be decreasing based on the thermal diffusion physical mechanism [52]. Since the shapes and sizes of elements from the low-fidelity FEA simulation are irregular, the re-heating usually cannot be simulated accurately compared with the high-fidelity FEA simulation. Therefore, as shown in Fig. 6, the FEA simulation results are truncated based on the input heat to guarantee that in each segment, no re-heating but only one thermal diffusion
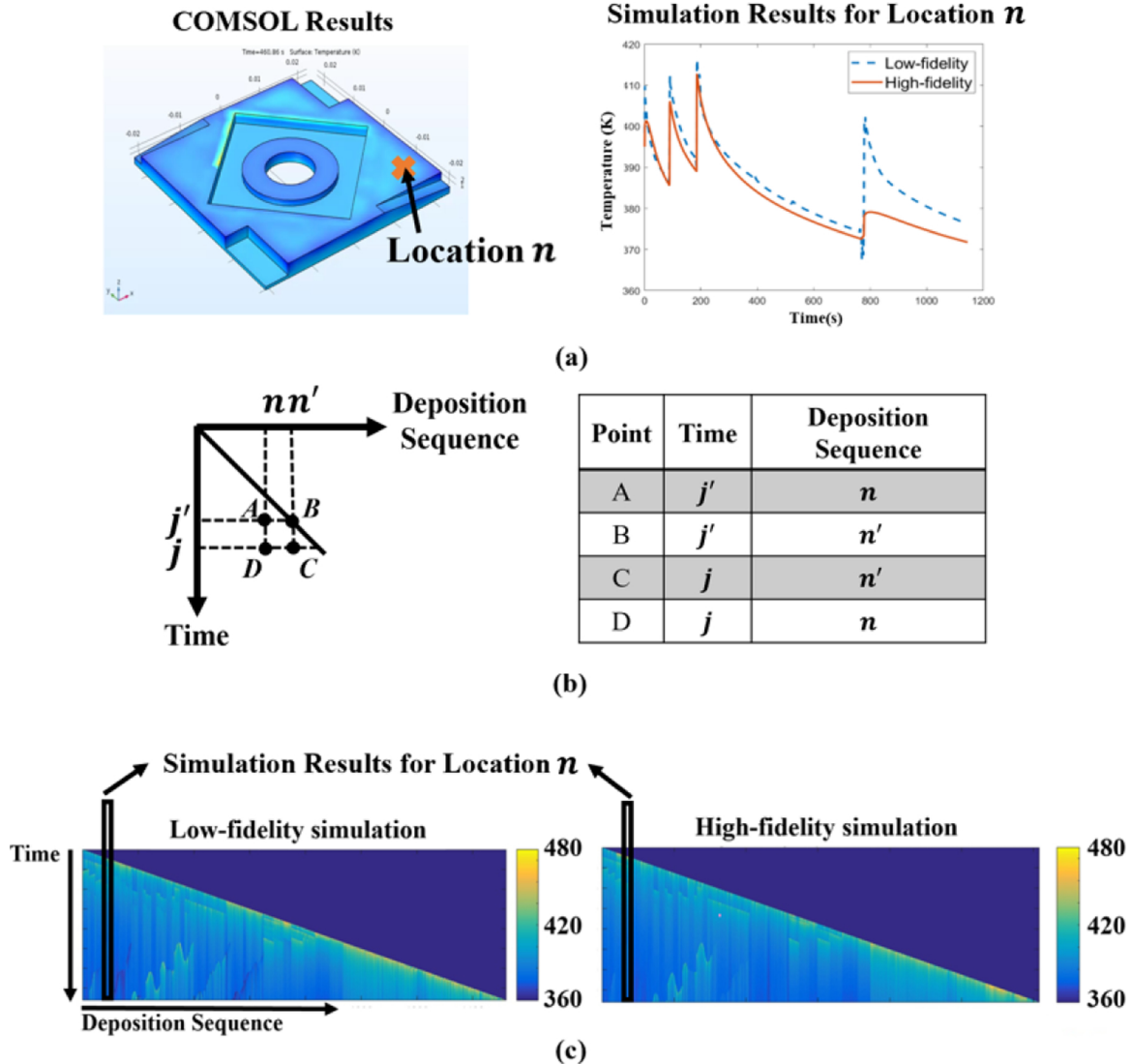

Fig. 5. (a) Examples of raw simulation results of temperature history of a voxel (location j) (b) The illustration of the lower triangular matrix. (c) Examples of lower triangular matrix for both low- and high-fidelity FEA simulation results.
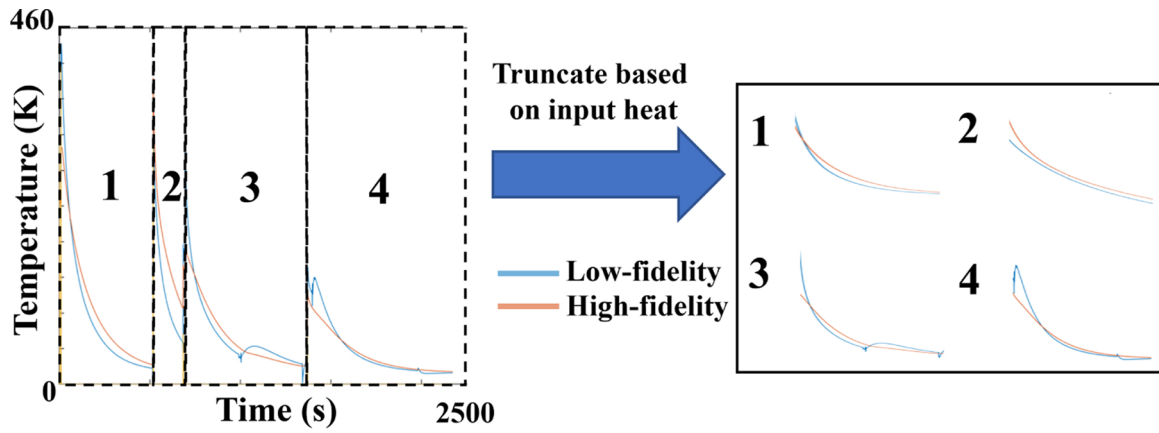
Fig. 6. Signal truncation according to the input heat information.

Table 3
Prediction performance for cross-layers scenario: Testing RMSEs (unit: K).

Design name	Lasso regression	Tensor regression	Functional linear regression	Variational autoencoder	Proposed
Standard	12.75	7.46	9.44	9.63	**4.32**
Peanut	10.51	6.58	7.07	11.64	**4.04**
Gear	12.49	9.71	8.53	9.63	**4.45**

Table 4
Prediction performance for cross-designs scenario: Testing RMSEs (unit: K)

Design Name	Lasso Regression	Tensor Regression	Functional Linear Regression	Variational Autoencoder	Proposed
Standard	15.14	11.41	10.72	12.91	**5.19**
Peanut	13.28	10.03	9.52	12.07	**4.84**
Gear	15.86	12.37	10.53	11.63	**5.67**

process exists. In the case study, each segment of simulation results is treated as one path (please note that the definition of a path is introduced in Section 1).

4.3. Model evaluation

To comprehensively evaluate the performance of the proposed model, two training-testing scenarios are employed: i) "cross-layers", which iteratively uses each one layer from each design as the training set, and the rest layers from the same design are used as testing set; and ii) "cross-designs", which iteratively uses all layers from each one design as the training set, and other two new designs are used as the testing set. These two scenarios can help validate whether the proposed model is able to accurately predict the simulation results for a new design (i.e., testing set) only based on the historical data (i.e., training set). The root-mean-square errors (RMSEs) are used to measure the prediction performance as: $\sqrt{\frac{\sum_{i=1}^{m}\sum_{j=1}^{l_i}(\hat{y}_{ij} - y_{ij})^2}{\sum_{i=1}^{m} t_i}}$. It represents the averaged errors of the predictions for paths from each location in different layers and designs. Based on distribution of ordinary least squares coefficients fitted from training data set, hyperparameters for priors can be identify. Specifically, in this case study, $[\alpha_0, \alpha_1] = [2, 2]$; $[\gamma_0, \gamma_1] = [1, 1]$; $\alpha_{01} = ... = \alpha_{0w} = \alpha_{11} = ... = \alpha_{1w} = 2$; $\gamma_{01} = ... = \gamma_{0w} = \gamma_{11} = ... = \gamma_{1w} = 1$; $a_0 = 0$; $b_0^2 = 0.2$; $a_1 = 0$; $b_1^2 = 0.5$; $\alpha_2 = 2$; $\gamma_2 = 1$.

To better demonstrate the advantages of the proposed method, four benchmarks are employed: (1) Lasso regression [46], which is a classical linear regression method. In the case study, all covariates and results from the low-fidelity FEA simulation are used as predictors; (2) tensor regression [47], which considers the local spatial and temporal correlation of paths. In the case study, the covariates among paths and the path from the low-fidelity FEA simulation results are formed as

matrices, and these matrices are further stacked as a tensor; (3) functional linear regression [18], which is a classical method for functional data analysis. In the case study, the path for each location from the low-fidelity FEA simulation results are treated as the predictors; and (4) VAE [48] which is a deep learning method aiming to generate dense representations of the path. In the case study, the long short term memory (LSTM) neural network structure is employed [53]. The encoder will first encode the low-fidelity FEA simulation results as dense vectors. Then, through the decoder, the corresponding high-fidelity FEA simulation results can be predicted.

4.4. Results and discussion

The RMSEs for two testing scenarios are shown in Tables 3 and 4, respectively. It can be observed that for both testing scenarios, the proposed method outperforms all benchmarks. The superior performance indicates that the proposed GPGP model can better model the heterogeneous discrepancies between low- and high-fidelity FEA simulation results because it employs the general path model to quantify the individual discrepancies for each path. It further adopts the Gaussian process model as constraints in coefficient estimation for general path models to enforce the similarity structure among model coefficients which can be quantified by design information and process information among paths. On the other hand, Lasso regression obtains the worst performance among all methods since it neither considers the spatial-temporal relationship among samples nor has dynamic model coefficients for different paths. Tensor regression has a better performance than Lasso regression since it can partially explain the heterogeneous discrepancy by demonstrating the spatial-temporal relationship, however, restricted by the size and dimension of the tensor, a limited proportion of discrepancy can be explained. Similarly, the
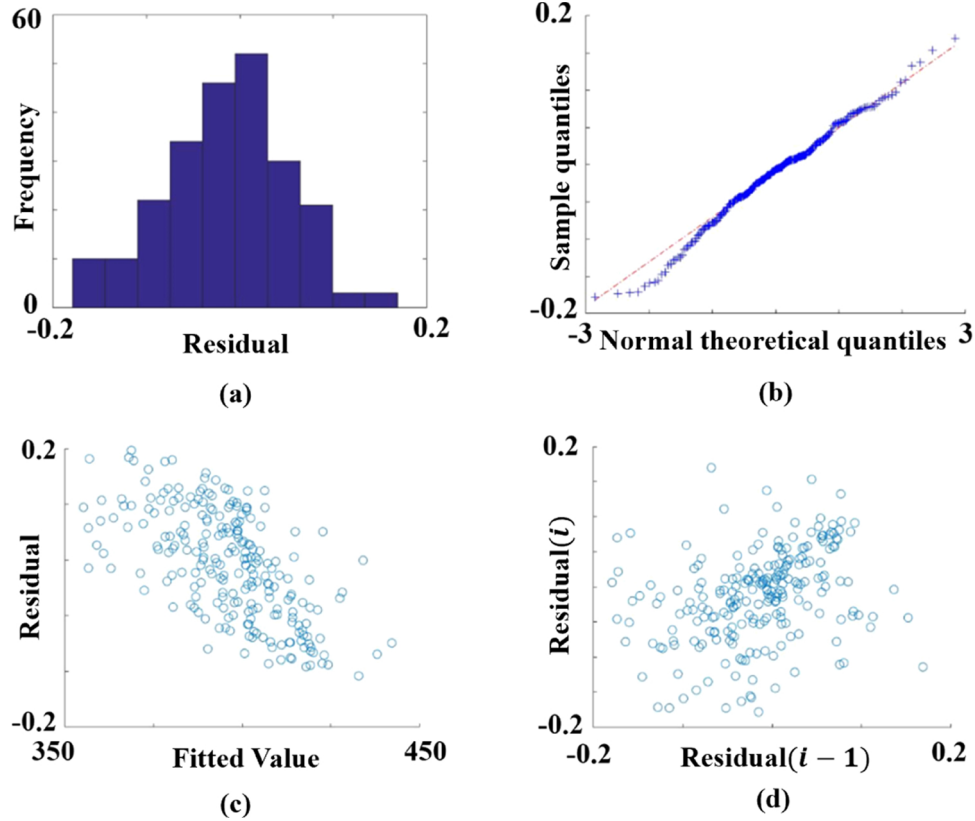
Fig. 7. Linear model assumption check for the proposed linear general path model ((a) histogram of residual; (b) Q-Q plot; (c) residuals vs. fitted values; (d) lag-1 residual plot).
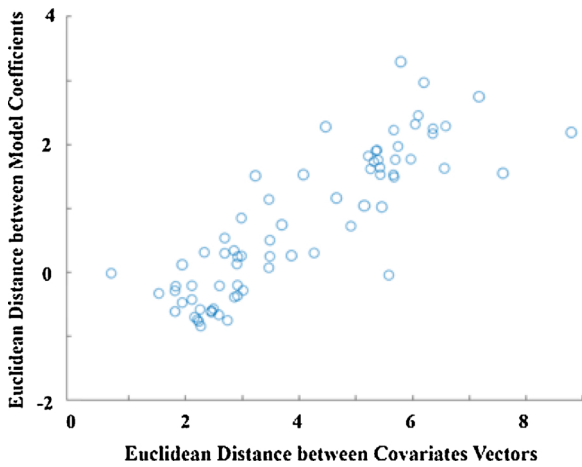

Fig. 8. Pair-wise correlation between covariates and model coefficients.

functional linear regression can better demonstrate the temporal relationship of the data. However, it is still difficult to provide a group of accurate basis functions for all paths since they are indeed heterogeneous. For VAE, it is difficult to involve the natural spatial-temporal correlation among paths due to the complex network structure to explicitly improve the performance of the model. Moreover, even it employed a more complex model structure, it may not be sufficient to comprehensively quantify the heterogeneous discrepancy among all paths without any interpretable model structure.

In order to validate the assumption that the relationship between low- and high-fidelity FEA simulation results can be modeled as a general path model with a first-order polynomial form, the residuals are checked based on the training results of the case study. Fig. 7 shows the

residual plot for a location from the standard design. It can be concluded that the residual (i.e., $y_{ij} - \widehat{y}_{ij}^*$ as defined in Section 2) of the general path model follows a normal distribution; the average of the residuals is close to zero; and the residuals are independent. These conclusions validate the assumption. On the other hand, it can be found that the residual term has heteroscedasticity which indicate the samples might have different variability across different locations on the product. One possible reason is that we only employ the first-order polynomial function for the general path model, whose performance is good enough comparing with the benchmarks. In future, we will investigate to optimize the general function form for the general path model based on heterogeneous discrepancies among paths. The heteroscedasticity might be also due to the numerical errors in low-fidelity FEA simulation results which introduce more disturbances in model estimation. This type of numerical errors directly relates to the characteristics of the simulation solver and FEA, which is out-of-scope in this study.

Moreover, to validate the assumption that there is a similarity structure among model coefficients of general path models, and this similarity can be represented by product design information and process design information, the correlation between covariates and model coefficients among different paths are presented in Fig. 8. In the figure, the Euclidean distance between covariates vectors is defined as $d_C = D(z_i, z_{i'})$ where z_i and $z_{i'}$ are the covariates vectors for path i and i' respectively. Similarly, the Euclidean distance among model coefficients is defined as $d_B = D([\beta_{i0}, \beta_{i1}]^\top, [\beta_{i'0}, \beta_{i'1}]^\top)$. From Fig. 8, it can be observed that if the distance between two covariates vectors becomes larger, the distance between the two sets of model coefficients will increase correspondingly, *vise versa*, which validates the assumption.

4.5. Application and limitations

The proposed GPGP model adopts general path models for the heterogeneous discrepancies between low- and high-fidelity FEA

simulation for each paths among locations. In order to apply the proposed model to boost the capability of FEA simulations in other case studies, a general function form (e.g., a polynomial function) to roughly approximate these discrepancies needs to be firstly identified manually or by fitting polynomial functions. Next, the covariates extracted from product design and process design are required to feed in Gaussian process model-based constraints to enforce the correlation structure of general path models among different paths. The covariates can be extracted from different sources of data such as product design information and process information. These covariates are expected to directly or indirectly correlate with the root-cause of heterogeneous discrepancies between low- and high-fidelity FEA simulation results. As a general method, the GPGP model can be readily extended to other types of simulation or data sets that satisfy all three assumptions, such as residual stress analysis [54], product strain and deviation analysis [55], etc.

However, limitations exist in the proposed model. First, this study does not investigate the lower bound of FEA fidelity levels (i.e., meshing resolutions in this study). For example, if the meshing resolution of the low-fidelity FEA simulation cannot provide rough thermal history trends in each location, the GPGP model may not accurately model heterogeneous discrepancies due to the lack of information. Furthermore, the proposed method shows the potential to identify the lower bound for FEA fidelity levels by setting a desired GPGP prediction accuracy and inversely optimizing the meshing size, which will be investigated in the future. Second, the pre-determined general function form (i.e., a first-order polynomial function in this study) may not be optimal. Tuning the selection of general function form requires the exploration of a few feasible functions, which may lead to a high computation workload in repeatedly estimating GPGP models with different general function forms. Although similar functions, in practice, result in similar prediction performance, automatically optimizing the general function form is expected to further improve the performance.

5. Conclusion

FEA has been widely adopted to validate the process and product design in AM to identify potential defects in AM process. Different fidelity levels for FEA are available to be implemented according to different objectives and demands. High-fidelity FEA simulation has satisfactory accuracy but yields high computation workload and huge time-consumption, which may not be affordable. On the other hand, low-fidelity FEA simulation is efficient but with limited capability in terms of accuracy. In this study, we propose a GPGP model to predict high-fidelity simulation results from low-fidelity simulation results by quantifying their heterogeneous discrepancies. In the GPGP model, we quantify these discrepancies through general path models. The relationships among model coefficients are constrained by a Gaussian process model via incorporating the product design information and process design information. The proposed method was validated in a real case study via a FDM process with three different designs for two training-testing scenarios (i.e., cross-layers and cross-designs). The results show that the proposed model outperforms the benchmark methods with validated assumptions in both scenarios. Therefore, it can boost capability of low-fidelity FEA simulation, especially to validate a new product and process design via boosted low-fidelity simulation with satisfactory accuracy in a timely manner. The independence from geometric designs and physical mechanisms enables GPGP model to be applied to other types of simulation or data sets that satisfy all three assumptions, such as residual stress analysis [54], product strain and deviation analysis [55], etc.

This paper leads to some future research directions. First, we will study the lower bounds of FEA fidelity levels by setting a desired GPGP prediction accuracy and inversely optimizing the meshing size. Next, we would like to investigate a spline regression model with variable

selection to optimize the general function form based on heterogeneous discrepancies. Moreover, we will validate more complex geometries of AM design and other types of AM processes such as lattice structure and SLM. Lastly, the proposed model might be possible to be combined with the computer experiment calibration to facilitate the accuracy improvement process by jointly estimating the calibration parameters and model coefficients under a hierarchical Gaussian process model framework [28].

References

[1] Hyunwoong Ko, Seung Ki Moon, Jihong Hwang, Design for additive manufacturing in customized products, Int. J. Precis. Eng. Manuf. 16 (11) (2015) 2369–2375.
[2] Rianne E. Laureijs, Jaime Bonnín Roca, Sneha Prabha Narra, Colt Montgomery, Jack L. Beuth, Erica R.H. Fuchs, Metal additive manufacturing: Cost competitive beyond low volumes, J. Manuf. Sci. Eng. 139 (8) (2017) 081010.
[3] Robert J. Morrison, Scott J. Hollister, Matthew F. Niedner, Maryam Ghadimi Mahani, Albert H. Park, Deepak K. Mehta, Richard G. Ohye, Glenn E. Green, Mitigation of tracheobronchomalacia with 3D-printed personalized medical devices in pediatric patients, Sci. Transl. Med. 7 (285) (2015) 285.
[4] I nigo Flores Ituarte, Eric Coatanea, Mika Salmi, Jukka Tuomi, Jouni Partanen, Additive manufacturing in production: A study case applying technical requirements, Proc. Proc. 78 (2015) 357–366.
[5] Haijun Gong, Khalid Rafi, Hengfeng Gu, Thomas Starr, Brent Stucker, Analysis of defect generation in Ti-6Al-4V parts made using powder bed fusion additive manufacturing processes, Addit. Manuf. 1 (2014) 87–98.
[6] K. Zakaria, Z. Ismail, N. Redzuan, K.W. Dalgarno, Effect of wire edm cutting parameters for evaluating of additive manufacturing hybrid metal material, Proc. Manuf. 2 (2015) 532–537.
[7] Michele Chiumenti, Xin Lin, Miguel Cervera, Wei Lei, Yuxiang Zheng, Weidong Huang, Numerical simulation and experimental calibration of additive manufacturing by blown powder technology Part I: Thermal analysis, Rapid Prototyping J. (2017).
[8] T.A. Krol, C. Seidel, M.F. Zaeh, Prioritization of process parameters for an efficient optimisation of additive manufacturing by means of a finite element method, Procedia Cirp 12 (2013) 169–174.
[9] Guglielmo Vastola, Gang Zhang, Q.X. Pei, Y.-W. Zhang, Controlling of residual stress in additive manufacturing of Ti6Al4V by finite element modeling, Addit. Manuf. 12 (2016) 231–239.
[10] Xiaoyu Chen and Ran Jin Data fusion pipelines for autonomous smart manufacturing. In 2018 IEEE 14th International Conference on Automation Science and Engineering (CASE).
[11] Y. Zhang, Y.K. Chou, Three-dimensional finite element analysis simulations of the fused deposition modelling process, Proc. Inst. Mech. Eng. Part B: J. Eng. Manuf. 220 (10) (2006) 1663–1671.
[12] Claire Benwood, Andrew Anstey, Jacek Andrzejewski, Manjusri Misra, Amar K. Mohanty, Improving the impact strength and heat resistance of 3D printed models: Structure, property, and processing correlationships during fused deposition modeling (FDM) of poly (lactic acid), ACS omega 3 (4) (2018) 4400–4411.
[13] Jingran Li, Ran Jin, Z. Yu Hang, Integration of physically-based and data-driven approaches for thermal field prediction in additive manufacturing, Mater. Design 139 (2018) 473–485.
[14] Prahalad K. Rao, Jia Peter Liu, David Roberson, Zhenyu James Kong, Christopher Williams, Online real-time quality monitoring in additive manufacturing processes using heterogeneous sensors, J. Manuf. Sci. Eng. 137 (6) (2015) 061007.
[15] Jerome Friedman, Trevor Hastie, Robert Tibshirani, The Elements of Statistical Learning, volume 1, Springer, New York, 2001.
[16] Haşim Sak, Andrew Senior, Françoise Beaufays, Long short-term memory recurrent neural network architectures for large scale acoustic modeling. In Fifteenth Annual Conference of the International Speech Communication Association (2014).
[17] Charoula Kousiatza, Nikoleta Chatzidai, Dimitris Karalekas, Temperature mapping of 3D printed polymer plates: Experimental and numerical study, Sensors 17 (3) (2017) 456.
[18] Fang Yao, Hans-Georg Müller, Jane-Ling Wang, Functional linear regression analysis for longitudinal data, Ann. Stat. 33 (6) (2005) 2873–2903.
[19] C. Joseph Lu, William O. Meeker, Using degradation measures to estimate a time-to-failure distribution, Technometrics 35 (2) (1993) 161–174.
[20] J.C. Heigel, P. Michaleris, Edward William Reutzel, Thermo-mechanical model development and validation of directed energy deposition additive manufacturing of Ti-6Al-4V, Addit. Manuf. 5 (2015) 9–19.
[21] Qian Chen, Xuan Liang, Devlin Hayduke, Jikai Liu, Lin Cheng, Jason Oskin, Ryan Whitmore, Albert C. To, An inherent strain based multiscale modeling framework for simulating part-scale residual deformation for direct metal laser sintering, Addit. Manuf. 28 (2019) 406–418.
[22] Sunil Bhandari, Roberto Lopez-Anido, Finite element analysis of thermoplastic polymer extrusion 3D printed material for mechanical property prediction, Addit. Manuf. 22 (2018) 187–196.
[23] Yi-Tang Kao, Ying Zhang, Jyhwen Wang, Bruce L. Tai, Bending behaviors of 3D-printed Bi-material structure: Experimental study and finite element analysis, Addit. Manuf. 16 (2017) 197–205.
[24] Mojtaba Mozaffar, Ebot Ndip-Agbor, Stephen Lin, Gregory J. Wagner,

Kornel Ehmann, Jian Cao, Acceleration strategies for explicit finite element analysis of metal powder-based additive manufacturing processes using graphical processing units, Comput. Mech. 64 (3) (2019) 879–894.

[25] Marc C. Kennedy, Anthony O'Hagan, Bayesian calibration of computer models, J. Roy. Stat. Soc.: Series B (Statistical Methodology) 63 (3) (2001) 425–464.

[26] Rui Tuo, C.F. Jeff Wu, et al., Efficient calibration for imperfect computer models, Ann. Stat. 43 (6) (2015) 2331–2352.

[27] Matthew Plumlee, Bayesian calibration of inexact computer models, J. Am. Stat. Assoc. 112 (519) (2017) 1274–1285.

[28] Dave Higdon, James Gattiker, Brian Williams, Maria Rightley, Computer model calibration using high-dimensional output, J. Am. Stat. Assoc. 103 (482) (2008) 570–583.

[29] Z.G. Peter, C.F. Qian, Jeff Wu, Bayesian hierarchical modeling for integrating low-accuracy and high-accuracy experiments, Technometrics 50 (2) (2008) 192–204.

[30] Robert B. Gramacy, Herbert K.H. Lee, Adaptive design and analysis of super-computer experiments, Technometrics 51 (2) (2009) 130–145.

[31] Haifeng Xia, Yu Ding, Bani K. Mallick, Bayesian hierarchical model for combining misaligned two-resolution metrology data, IIE Transactions 43 (4) (2011) 242–258.

[32] Shifeng Xiong, Z.G. Peter, C.F. Qian, Jeff Wu, Sequential design and analysis of high-accuracy and low-accuracy computer codes, Technometrics 55 (1) (2013) 37–46.

[33] Mostafa Reisi Gahrooei, Kamaran Paynabar, Massimo Pacella, Bianca Maria Colosimo, An adaptive fused sampling approach of high-accuracy data in the presence of low-accuracy data, IISE Transactions 51 (11) (2019) 1251–1264.

[34] Qiang Huang, An analytical foundation for optimal compensation of three-dimensional shape deformation in additive manufacturing, J. Manuf. Sci. Eng. 138 (6) (2016) 061010.

[35] He Luan, Marco Grasso, Bianca M. Colosimo, Qiang Huang, Prescriptive data-analytical modeling of laser powder bed fusion processes for accuracy improvement, J. Manuf. Sci. Eng. 141 (1) (2019) 011008.

[36] Arman Sabbaghi, Qiang Huang, Tirthankar Dasgupta, Bayesian model building from small samples of disparate data for capturing in-plane deviation in additive manufacturing, Technometrics 60 (4) (2018) 532–544.

[37] Y. Zhang, K. Chou, A parametric study of part distortions in fused deposition modelling using three-dimensional finite element analysis, Proceedings of the Institution of Mechanical Engineers, Part B: Journal of Engineering Manufacture 222(8) (2008) 959–968.

[38] Thomas J.R. Hughes, The finite element method: Linear static and dynamic finite element analysis, Courier Corporation, Chelmsford, MA, 2012.

[39] James Douglas Hamilton, Time series analysis, volume 2, Princeton university press, Princeton, NJ, 1994.

[40] Andrew Gelman, Jennifer Hill, Data analysis using regression and multilevel/hierarchical models, Cambridge university press, Cambridge, England, 2006.

[41] Thomas J. Santner, Brian J. Williams, William Notz, The design and analysis of computer experiments, volume 1, Springer, New York, 2003.

[42] Charles A. Micchelli, Yuesheng Xu, Haizhang Zhang, Universal kernels, J. Mach. Learn. Res. 7 (Dec) (2006) 2651–2667.

[43] Christopher K.I. Williams, Carl Edward Rasmussen, Gaussian processes for machine learning, volume 2, MIT press, Cambridge, MA, 2006.

[44] Andrew Gelman, et al., Prior distributions for variance parameters in hierarchical models (comment on article by browne and draper), Bayesian Anal. 1 (3) (2006) 515–534.

[45] Matthew D. Hoffman, Andrew Gelman, The no-u-turn sampler: Adaptively setting path lengths in hamiltonian monte carlo, Journal of Machine Learning Research 15 (1) (2014) 1593–1623.

[46] Robert Tibshirani, Regression shrinkage and selection via the lasso, J. Roy. Stat. Soc.: Ser. B (Methodological) 58 (1) (1996) 267–288.

[47] Hua Zhou, Lexin Li, Hongtu Zhu, Tensor regression with applications in neuroimaging data analysis, J. Am. Stat. Assoc. 108 (502) (2013) 540–552.

[48] Diederik P Kingma and Max Welling Auto-encoding variational bayes. arXiv preprint arXiv:1312.6114, 2013.

[49] Liang Bo Ji, Tian Rui Zhou, Finite element simulation of temperature field in fused deposition modeling, Adv. Mater. Res. 97 (2010) 2585–2588.

[50] Yvan Dutil, Daniel R. Rousse, Nizar Ben Salah, Stéphane Lassue, Laurent Zalewski, A review on phase-change materials: Mathematical modeling and simulations, Renew. Sustain. Energy Rev. 15 (1) (2011) 112–130.

[51] Jie Zhang, Xin Zhou Wang, Wang Wang Yu, Yu He Deng, Numerical investigation of the influence of process conditions on the temperature variation in fused deposition modeling, Mater. Design 130 (2017) 59–68.

[52] M. Nikzad, S.H. Masood, I. Sbarski, Thermo-mechanical properties of a highly filled polymeric composites for fused deposition modeling, Mater. Des. 32 (6) (2011) 3448–3456.

[53] Sepp Hochreiter, Jürgen Schmidhuber, Long short-term memory, Neural Comput. 9 (8) (1997) 1735–1780.

[54] Caterina Casavola, Alberto Cazzato, Vincenzo Moramarco, Giovanni Pappalettera, Residual stress measurement in fused deposition modelling parts, Polym. Testing 58 (2017) 249–255.

[55] Miquel Domingo-Espin, Josep M. Puigoriol-Forcada, Andres-Amador Garcia-Granada, Jordi Llumà, Salvador Borros, Guillermo Reyes, Mechanical property characterization and simulation of fused deposition modeling polycarbonate parts, Mater. Design 83 (2015) 670–677.